

pubs.acs.org/JACS Article

High-Performance Lithium—Sulfur Batteries via Molecular Complexation

Peiyu Wang, Nikolaos Kateris, Baiheng Li, Yiwen Zhang, Jianmin Luo, Chuanlong Wang, Yue Zhang, Amitesh S. Jayaraman, Xiaofei Hu, Hai Wang,* and Weiyang Li*



Cite This: J. Am. Chem. Soc. 2023, 145, 18865-18876





ABSTRACT: Beyond lithium-ion technologies, lithium—sulfur batteries stand out because of their multielectron redox reactions and high theoretical specific energy (2500 Wh kg⁻¹). However, the intrinsic irreversible transformation of soluble lithium polysulfides to solid short-chain sulfur species (Li_2S_2 and Li_2S) and the associated large volume change of electrode materials significantly impair the long-term stability of the battery. Here we present a liquid sulfur electrode consisting of lithium thiophosphate complexes dissolved in organic solvents that enable the bonding and storage of discharge reaction products without precipitation. Insights garnered from coupled spectroscopic and density functional theory studies guide the complex molecular design, complexation mechanism, and associated electrochemical reaction mechanism. With the novel complexes as cathode materials, high specific capacity (1425 mAh g⁻¹ at 0.2 C) and excellent cycling stability (80% retention after 400 cycles at 0.5 C) are achieved at room temperature. Moreover, the highly reversible all-liquid electrochemical conversion enables excellent low-temperature battery operability (>400 mAh g⁻¹ at -40 °C and >200 mAh g⁻¹ at -60 °C). This work opens new avenues to design and tailor the sulfur electrode for enhanced electrochemical performance across a wide operating temperature range.

■ INTRODUCTION

Modern lithium-ion batteries have successfully enabled rechargeable and mobile energy storage since the 1990s. While in practical battery applications, conventional lithium intercalation-based chemistry is approaching its theoretical capacity limit, the emergence of electric vehicles and grid energy storage need calls for more energy-dense and lower-cost battery options.²⁻⁴ As a known cathode material, elemental sulfur is abundant, inexpensive, and nontoxic; it also possesses a high theoretical capacity of 1672 mAh g^{-1,4,5} By pairing a sulfur cathode with a metallic lithium anode, a lithium-sulfur (Li-S) battery can theoretically provide a specific energy of 2500 Wh kg^{-1.6} For this reason, it has been considered a promising path to meeting future energy storage requirements. 4-6 A typical Li-S battery discharge process undergoes multiphase redox reactions, with reactants, intermediates, and products ranging from solid sulfur to soluble long-chain lithium polysulfides, to insoluble Li₂S₂/Li₂S.^{7,8} Such a chemical process has multiple issues, including the shuttle effect, low

conductivities of solid sulfur species (S, Li₂S₂, and Li₂S), and large volume changes of the sulfur electrode (\sim 80%). These issues lead to a range of undesirable battery chemistry, from sluggish reaction kinetics to irreversibility, and hence poor Coulombic efficiency, capacity, and cycle life. Further, these problems are exacerbated for energy storage applications in cold climates where the battery is operated below 0 °C. $^{9-11}$

To date, extensive efforts have been made to trap soluble polysulfides in order to mitigate their dissolution and shuttle effect. Proposed methods include the use of confined carbonaceous frameworks 13-16 and electrode/electrolyte additives 17-20 as well as deploying chemical catalysis. 21-24

Received: May 19, 2023 Published: August 17, 2023





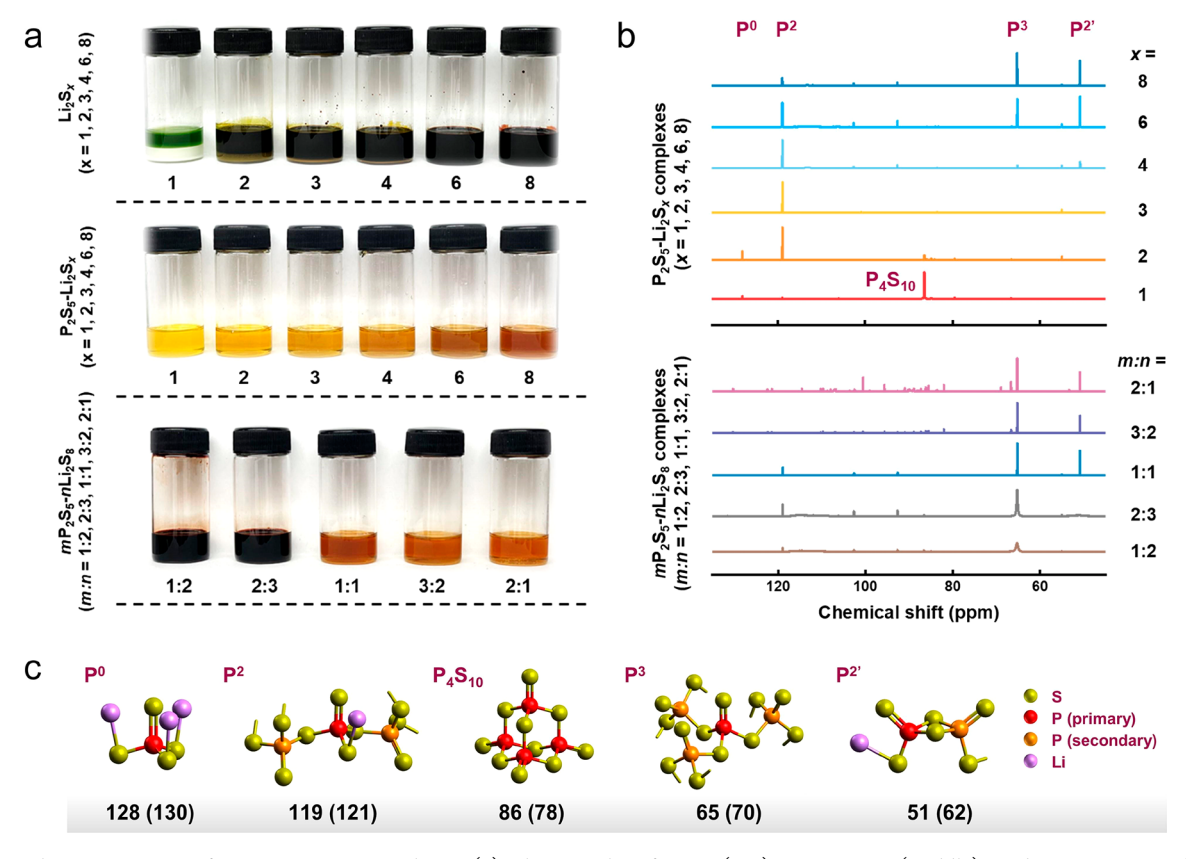


Figure 1. Characterizations of $mP_2S_5-nLi_2S_x$ complexes. (a) Photographs of Li_2S_x (top), $P_2S_5-Li_2S_x$ (middle), and $mP_2S_5-nLi_2S_8$ (bottom) complexes dissolved in TEGDME; the amount of solvent is fixed at 80 wt %. (b) ^{31}P NMR characterization of $P_2S_5-Li_2S_x$ and $mP_2S_5-nLi_2S_8$ complexes. (c) Corresponding phosphorus short-range order structures with experimental (and theoretically predicted) chemical shifts. In the case of dissimilar P atoms, the primary P is shown in a darker color.

Recently, various functionalized metal-organic framework (MOF) and covalent-organic framework (COF) materials were also developed to chemically tether soluble polysulfides with enhanced cell reversibility and capacity delivery. ^{25–28} On the other hand, much less attention has been placed on controlling the precipitation of solid Li₂S₂/Li₂S. The irreversible precipitation of Li₂S₂/Li₂S not only leads to the loss of active materials but also causes large charging overpotentials and blocks the charge transfer pathway in cathodes, hence reducing the utilization and practical capacity of the sulfur electrode.²⁹ The significant volume change of the sulfur electrode also produces mechanical stress in the battery cell and weakens the electrode mechanically. 30,31 A possible path to resolving the above issues is to render Li₂S₂/Li₂S soluble during battery operation. For example, ammonium salts were demonstrated as effective additives to promote the dissolution of Li_2S in dimethyl sulfoxide. ³² An ε -caprolactam/ acetamide-based eutectic solvent was reported to dissolve lithium polysulfides and lithium sulfide with improved battery cycling performance.³³

Herein, we introduce a unique lithium thiophosphate complexation chemistry and show that as battery catholytes lithium thiophosphate complexes successfully accommodate discharge products ($\text{Li}_2\text{S}_2/\text{Li}_2\text{S}$) that would otherwise precipitate. Specifically, we found that the complexation of P_2S_3 and lithium polysulfides (Li_2S_x) establishes multiple tetrahedral phosphorus(V) centers, which are capable of bridging polysulfide chains of varying lengths through phosphorus—sulfur (P–S) coordination or covalent interaction. Coupled

experimental characterization and theoretical density functional theory (DFT) calculations at the uB3LYP/6-31+G-(2df,p) level of theory^{34–38} were conducted to formulate the complex structures and to understand the underlying complexation and electrochemical reaction mechanisms. The novel complexation chemistry was shown to prevent discharge products from precipitating during the battery operation. At room temperature, the specific capacity measured on the basis of active sulfur was 1425 mAh g⁻¹ at 0.2 C charge/discharge rate, and the capacity remained at 1270 mAh g⁻¹ after 200 cycles. Under a charge/discharge rate of 0.5 C, the cathode exhibited 80% of capacity retention after 400 cycles. Moreover, the enhanced electrochemical activities and all-liquid reaction kinetics enable the cell operability to reduced temperatures $(>400 \text{ mAh g}^{-1} \text{ at } -40 \text{ }^{\circ}\text{C} \text{ and } >200 \text{ mAh g}^{-1} \text{ at } -60 \text{ }^{\circ}\text{C}),$ which offers great promise for enabling practical Li-S batteries with wide-range temperature operability.

■ RESULTS AND DISCUSSION

Molecular Design. Lithium thiophosphates were synthesized by reacting lithium sulfide (Li₂S), sulfur, and P_2S_5 powders in tetraethylene glycol dimethyl ether (TEGDME) under mild conditions (see Methods section, Supporting Information). The as-prepared complex solutions are denoted as $mP_2S_5-nLi_2S_x$ ($1 \le x \le 8$). As such, the chemical compositions of the complexes are tailored in two separate dimensions—the S_x chain length (x) and the P_2S_5 :Li₂ S_x molar ratio (x)—to attain distinctive physicochemical and electrochemical properties. Solvent modification was also considered

Scheme 1. Proposed Complexation Mechanisms: (a) Initial Complexation of P_4S_{10} and $2Li_2S_x$ (m:n=1:1) Yields a Four-Atom Phosphorus Unit Structure with $P^{2'}$, $P^{2''}$, P^3 , and P^2 SROs; (b) Complexation of $3P_2S_5$ and $2Li_2S_x$ (m:n=3:2) Forms a Six-Atom Phosphorus Unit Structure with $P^{2'}$, $P^{2''}$, and P^3 SROs^a

^aBoth stoichiometries undergo ring-opening upon complexation with neighboring structures.

and demonstrated in low-temperature experiments. Figure 1a shows photographs of vials of various solutions of Li_2S_x ($1 \le x$ \leq 8) prepared in TEGDME without and with P₂S₅ addition. The solubility of Li_2S_x shows a strong dependency on the S_x chain length (Figure 1a, top). Long-chain polysulfides (x = 4, 6, and 8) are, in general, more soluble, showing characteristic dark red-brown colors. Short-chain polysulfides ($x \le 3$), on the other hand, exhibit limited solubilities. The addition of stoichiometric P_2S_5 (m:n = 1:1) allows otherwise insoluble or partially soluble Li₂S_x species to be completely soluble, producing clear and homogeneous solutions that vary in color from yellow to brown with an increased S_x chain length (Figure 1a, middle). No precipitation was found for all stoichiometric ratios tested with $S_{x=8}$ chains; these include m:n = 1:2, 2:3, 3:2, and 2:1 in addition to m:n = 1:1. However, m:n= 1:2 and 2:3 led to incomplete complexation, as evidenced by the distinct color differences seen in the bottom panel of Figure 1a. Note that P₂S₅ alone has limited solubility in TEGDME (Figure S1, Supporting Information). Also, octasulfur (S₈) with cyclic eight-membered rings cannot

complex with P_2S_5 in TEGDME due to the absence of terminal sulfide anions (Figure S2).

Characterization of $mP_2S_5-nLi_2S_x$ Complexes. To understand the complexation chemistry, we followed the common protocols in studies of glassy thiophosphate materials $^{39-42}$ and characterized the molecular structures in $mP_2S_5-nLi_2S_x$ complexes in terms of phosphorus short-range order structures (SROs) identifiable in the 31P nuclear magnetic resonance (NMR) spectra (Figure 1b). Extensive DFT calculations were also performed to identify the geometry of P-SROs (Figure S3 and Table S1) and the corresponding chemical shifts (Tables S2 and S3). Figure 1c presents the identified SROs, namely, P0, P2, P4S10, P3, and P2', with theoretical results matching the NMR spectra of Figure 1b. Essentially, each of the P-SROs corresponds to a local phosphorus bonding environment. For example, P³, the most prominent structure observed in long-chain complexes, refers to a short-range-order structure, wherein a particular phosphorus atom is bonded to three other phosphorus atoms via bridging sulfur atoms. The occurrence of P^{2r}

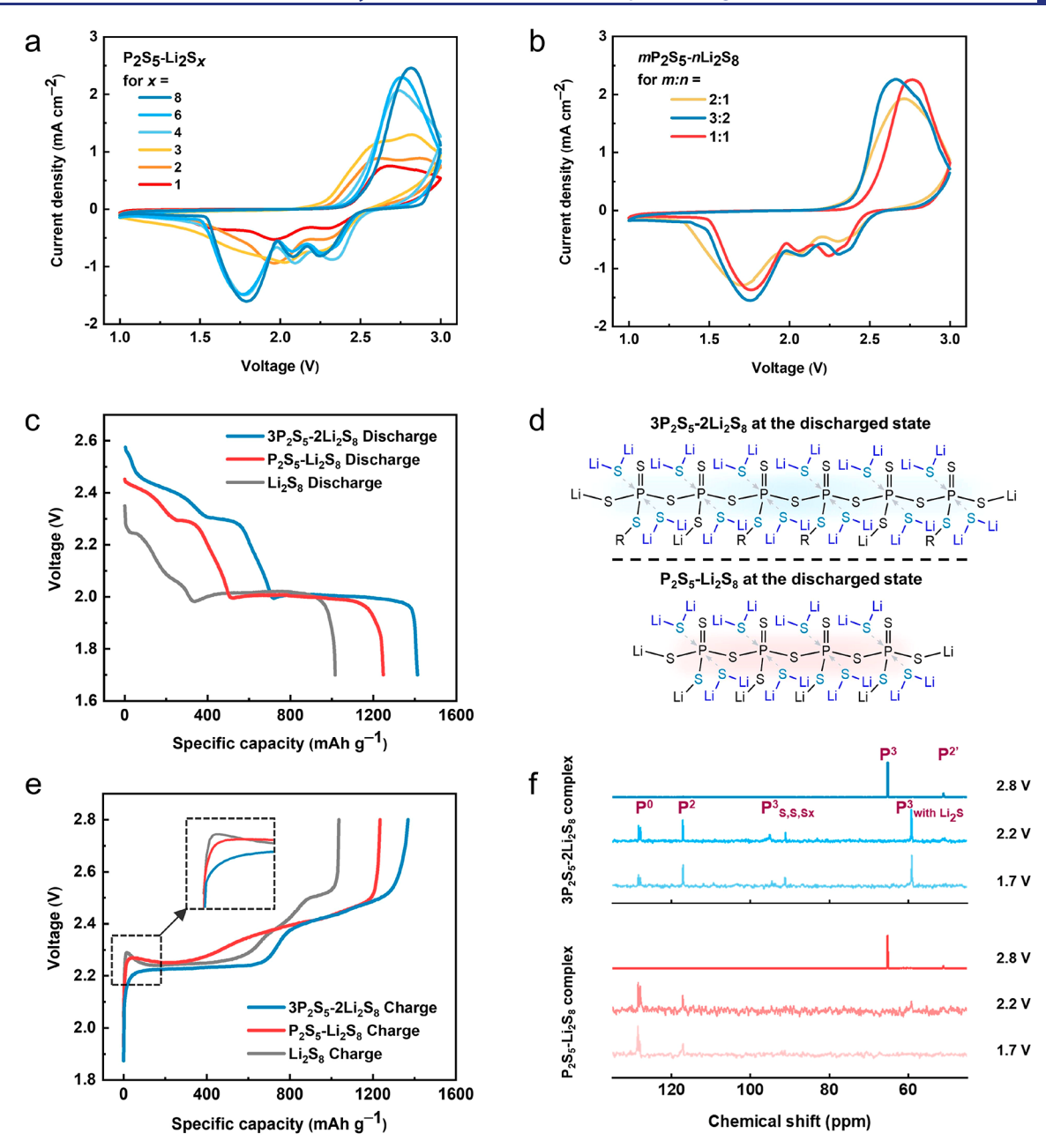


Figure 2. Electrochemical performance evaluation at room temperature. (a) CV profiles of cells with P_2S_5 —Li $_2S_8$ complexes at a scan rate of 0.1 mV s⁻¹. (b) CV profiles of cells with mP_2S_5 — nLi_2S_8 complexes at a scan rate of 0.1 mV s⁻¹. (c) Typical galvanostatic discharging voltage profiles of cells with $3P_2S_5$ — $2Li_2S_8$, P_2S_5 — Li_2S_8 , and Li_2S_8 catholytes at 0.1 C. (d) Proposed molecular structures of complexes at the discharged state (top: sixatom phosphorus unit structure associated with the $3P_2S_5$ — $2Li_2S_8$ complex). Sulfur atoms in light blue indicate accommodated active sulfur. R groups refer to either a terminal Li or another P-SRO. (e) Typical galvanostatic charging voltage profiles of cells with $3P_2S_5$ — $2Li_2S_8$, P_2S_5 — Li_2S_8 , and Li_2S_8 catholytes at 0.1 C. The inset shows the enlarged area of the initial charging process. (f) Ex situ ^{31}P NMR characterization of $3P_2S_5$ — $2Li_2S_8$ and P_2S_5 — Li_2S_8 catholytes held at different potentials over a 5 h period.

indicates the presence of a four-membered ring structure. Shorter chain complexes exhibit P^2 and P^0 instead, thus having more sulfur atoms terminated by Li than P^3 . In the case of P_2S_5 –Li₂S, P^2 and P^0 are still observed but are dwarfed by the P_4S_{10} peak. The presence of P_4S_{10} may be attributed to the slow complexation reaction kinetics between Li₂S and P_2S_5 (the monomer of P_4S_{10}), as the Li–S bond in Li₂S is strong and not readily dissociated by the solvent molecules. As for high m:n ratios, excessive P_2S_5 tends to react with P^2 to form higher-order $P^{2'}$ and P^3 networks, leading to the disappearance of the P^2 resonance in the NMR spectra. For lower m:n ratios,

on the other hand, reduced P_2S_5 leads to less complexation and an increased level of P–S termination by Li. This amplifies the P^2 intensity and reduces the $P^{2\prime}$ (and even P^3) connectivity.

Complementary Raman characterization confirmed the presence of P-SROs and S_x chains in the complexes as well as their chemical interactions. Comparing the spectra shown in Figures S4 and S5, the characteristic peaks of reactants disappear, and new peaks arise upon complexation. As indicated in Figure S5, the 482 cm⁻¹ peak is associated with the -S-S- stretching vibrations of the S_x chains in the complexes, while the peak at \sim 575 cm⁻¹ is assigned to the T_2

stretching of tetrahedral units in all SROs,⁴⁵ which shifts to lower energies with an increased S_x chain length, suggesting the interconnection between SRO units and S_x chains.^{41,42} The peak at 386 cm⁻¹ corresponds to P^2 and/or P^3 SROs,^{45,46} and that near 200 cm⁻¹ may be ascribed to P^3 .^{45,47} The 250 cm⁻¹ peak reveals P^2 ′ for the long-chain complexes.⁴⁵ An additional peak at ~300 cm⁻¹ indicates P^0 in short-chain complexes.⁴⁵

The complexation of P_2S_5 and Li_2S_r is solvent dependent to an extent. In addition to TEGDME, complexation occurs in selected ether-based solvents, including 1,2-dimethoxyethane (DME) and diethylene glycol dimethyl ether (DEGDME) (Figure S6). However, the molar concentration (or weight percent) of dissolved complex species in DME or DEGDME is smaller than that in TEGDME. The ¹H NMR spectra show no chemical reaction between TEGDME and the complex (Figure S7). Hence, the improved solvation in TEGDME is the result of its dielectric constant (ε = 7.9) being higher than DME (ε = 7.2) and DEGDME (ε = 7.3). 43,48 Both P₂S₅-Li₂S₈ and 3P₂S₅-2Li₂S₈ complex solutions in TEGDME exhibit good stability, as evidenced by their ³¹P and ¹H NMR spectra, which remain unchanged over 30 days of storage. However, the 2P₂S₅-Li₂S₈ complex shows an additional phosphorus peak after extended storage, which suggests potential negative effects from overdosing reactive P₂S₅ (Figures S8 and S9).

Complexation Mechanism. P₂S₅ generally exists in its dimer state, P₄S₁₀, in an adamantane-like cage structure. ⁴⁵ The dissociation of P₄S₁₀ readily produces P₂S₅ (Figure S10). As shown in Scheme 1a, which outlines the complexation mechanism of P_2S_5 -Li₂S₈ (or P_4S_{10} -2Li₂S₈), a pair of P-S bonds in P₄S₁₀ are attacked initially by two separate Li₂S_x molecules. The Li atom bonds with the S atoms from the broken P-S bonds, and the long sulfur chains (S_x) attach themselves onto P atoms. The resulting structure contains a six-membered P₃S₃ ring attached to the fourth P atom and two long sulfur chains terminated by Li. An isomerization reaction follows, in which a P-S bond in the six-membered ring is broken by a S-Li group, in a manner similar to the initial step of the complexation mechanism. This leads to an open fourphosphorus-atom configuration, consisting of four SROs: P2', P²", P³, and P². As shown in Figure S3 and Table S1, the P²' and P2" SROs correspond to P in four-membered P-S rings. The P³ SRO corresponds to P covalently bonded to three other P atoms via S bridges, and the P2 SRO corresponds to a P atom bound to two other P atoms and one Li atom via S bridges. An additional P₂S₅ molecule may react with the resulting four-P atom structure in the 3P₂S₅-2Li₂S₈ stoichiometry via sequential nucleophilic additions, as shown in Scheme 1b. A negatively charged S atom from P₂S₅ binds with Li and the positively charged P atom binds with S, extending the four-P atom structure into a six-P atom structure. A second nucleophilic addition (isomerization) step leads to the formation of a P-S four-membered ring, and the final six-P atom unit structure has two P3 SROs, associated with fully bridged P atoms, and two pairs of P2' and P²" SROs, associated with P-S rings. The absence of the P² SRO in the 3P₂S₅-2Li₂S₈ stoichiometry is also evident in the NMR spectrum of Figure 1b.

Not shown in Scheme 1 is the possible reaction of the other end of the polysulfide chain. While one end of the Li_2S_x is anchored onto the P–S backbone, the other end is capable of networking with neighboring structures (Figure S11) following the same mechanism as depicted in Scheme 1 and producing higher-dimensional complex structures with S_x chains as the

cross-links (Figure S12). In these structures, P^3 is the dominant SRO because all P atoms are interconnected via S bridges. Long S_x chains enable both intermolecular binding and, more importantly, intramolecular isomerization owing to their smaller steric hindrances, whereas short S_x chains favor intermolecular binding only. For this reason, a small m:n ratio is expected to reduce the higher-order connectivity and hence increase the intensities of the P^2 resonance and reduce $P^{2'}$ and P^3 contributions (Figure 1b). Overdosing P_2S_5 (e.g., $2P_2S_5$ — Li_2S_x), on the other hand, produces undesirable electrochemical properties because of the undesirable reactivity of excess P_2S_5 , as will be discussed later. The complexation mechanism proposed for m:n ratios other than 1:1 and 3:2 can be found in Figures S13—S15.

Electrochemical Reaction Mechanism. We evaluate the electrochemical properties and associated electrochemical mechanisms of the $mP_2S_5-nLi_2S_x$ complexes next in a coin cell configuration using a Li metal anode and conductive carbon paper as the cathode current collector (Figure S16). In each coin cell, a 40 μ L catholyte solution was added to the carbon paper as the cathode material. Figure 2a shows the cyclic voltammetry (CV) profiles of the P_2S_5 -Li₂S_x (1 $\leq x \leq$ 8) complexes. It can be seen that longer S_x chains give higher current densities. Also, long-chain complexes (x = 6, 8) exhibit four reduction peaks, contrary to the Li₂S₈ catholyte, which exhibits three reduction peaks under the same condition (see Figure S17). In addition, the reduction peak at low potential (1.84 V) tends to be appreciably larger for the complexes than Li_2S_8 without complexation (1.20 vs 0.47 mA cm⁻²), suggesting that the electrochemical reactivity of short-chain sulfur species is enhanced also with the P₂S₅ complexation.

Moreover, the m:n ratio in $mP_2S_5-nLi_2S_8$ has a notable effect on the electrochemical activities, as shown in Figure 2b. Specifically, the 3P₂S₅-2Li₂S₈ complex exhibits somewhat better electrochemical reactivity over the stoichiometric P₂S₅-Li₂S₈ complex; it allows for a slightly higher current density during reduction (e.g., 1.37 vs 1.20 mA cm⁻² for the lowest voltage discharge peak at 1.75 V). In addition, the shift of the oxidation peak to a lower potential (2.65 vs 2.76 V) suggests faster reaction kinetics in $3P_2S_5-2Li_2S_8$ than in the stoichiometric P₂S₅-Li₂S₈. However, when the m:n ratio is further increased from 3:2 to 2:1, we observed deteriorating electrochemical activities: the oxidation peak shifted back to a higher voltage (2.72 V), and the discharge voltage and current density both decreased to some extent. This indicates that an optimal stoichiometry exists for the complex; excess P2S5 beyond a certain level does not offer added benefits. A full comparison of the CV profiles of the complexes and Li₂S₈ catholytes under different scan rates is shown in Figure S17; the results over the range of scan rates are entirely consistent with those shown in Figure 2b. A corresponding Randles-Sevcik analysis suggests that, in general, the complex-based catholytes have a better Li+ diffusion rate during both reduction and oxidation processes compared to the Li2S8 catholyte without P₂S₅ complexation (Figure S18).

Several insights can be garnered by examining the voltage profiles by comparing the complexes and Li_2S_8 catholytes cycled between 1.7 and 2.8 V. As shown in Figure 2c, complexation shifts the potential at open circuit and the discharge plateaus (above 2.0 V) to higher values. Also, the complexes with enhanced electrochemical activities and diffusion rates render more complete reactions associated with each discharge plateau than Li_2S_8 without complexation,

leading to improved discharge capacities (1412, 1248, and 1015 mAh g^{-1} for $3P_2S_5-2Li_2S_8$, $P_2S_5-Li_2S_8$, and Li_2S_8 , respectively). In relation to the attractive electrochemical properties, bonding discharge products onto the complex network is the key effect of the complexation chemistry. As shown in Figure 2d, we propose that the four- and six-atom phosphorus unit structures formed by m:n = 1:1 and 3:2 complexation, respectively, have different capabilities of accommodating solid Li₂S at the discharged state. These structures arise from the final structures of Scheme 1, following the networking with neighboring structures, Sx chain shortening during discharge, and Li₂S accommodation. Ideally, the m:n = 3:2 complexation can anchor all 16 S atoms from 2Li_2S_8 through covalent bonding or ring-opening (Figure 2d, top). In contrast, the m:n = 1:1 complexation can accommodate 11 out of 16 active S atoms from 2Li₂S₈ onto its P-S backbone (Figure 2d, bottom). Detailed information on the number of accommodated Li₂S discharge molecules for different m:n ratios can be found in Figure S19. In fact, this difference underscores all property and performance differences that need to be discussed. In particular, the 3P₂S₅-2Li₂S₈ complex enables full Li₂S anchoring without excess P₂S₅; it effectively reduces the overpotential during the charging process compared to the stoichiometric P₂S₅-Li₂S₈ and Li₂S₈ catholytes (see Figure 2e). The voltage profile of the 2P₂S₅-Li₂S₈ complex was also tested (Figure S20), showing no notable improvement in electrochemical performance over the 3P₂S₅-2Li₂S₈ complex, as the excess P₂S₅ deteriorates Li⁺ diffusion rates (Figure S18).

To shed light on the molecular structures at different charged and discharged states as well as during the discharge process, we present the corresponding NMR characterizations of complexes in Figure 2f. The NMR spectra were taken ex situ after a cell was held at a certain potential over a 5 h period (see the Methods section). It is seen that the P3 SRO is the dominant structure at the charged state of 3P₂S₅-2Li₂S₈, as well as upon discharge, with the difference being that its chemical shift is slightly reduced due to the accommodation of Li₂S molecules onto the complex structure, as evaluated and confirmed by DFT calculations (see Table S3). P² and P⁰ are also present at the discharged state, arising from the shortening of edge sulfur chains, thus giving rise to Li-terminated phosphorus. In the case of the stoichiometric P₂S₅-Li₂S₈ complex, the dominant SRO is P⁰ during discharge instead. The presence of P^2 is explicable in the same way as for $3P_2S_5$ 2Li₂S₈ and is identifiable in the molecular structures in Figure 2d. The prominent P⁰ peak during discharge indicates that a significant fraction of phosphorus is isolated from larger complexes, as it is terminated by Li. In this process, a necessary step is the cleavage of P-S-P sequences, and this may occur spontaneously upon Li₂S addition (see Figure S21), as confirmed by the DFT calculation showing a corresponding Gibbs free energy of -2.2 eV.

To verify the reversibility of the cathode chemistry, carbon paper substrates that hold complex solutions (for *ex situ* NMR analysis) were then washed and dried for scanning electron microscopy (SEM) and energy-dispersive X-ray spectroscopy (EDS) characterization (Figures S22 and S23). For comparison, the Li₂S₈ catholyte was also subject to surface characterization under the same conditions (Figure S24). At 1.7 V, neither the 3P₂S₅-2Li₂S₈ nor the P₂S₅-Li₂S₈ catholyte exhibits apparent solid precipitation. However, irreversible precipitation of Li₂S was evident for the Li₂S₈ catholyte. In

addition, no solid S was observed at 2.8 V for the complex catholytes. If the long polysulfide chains are oxidized to solid S, then no characteristic SROs would be observed at 2.8 V in Figure 2f, but this is not the case. The results, therefore, indicate that the complex catholytes can be cycled reversibly between 1.7 and 2.8 V. In contrast, the Li_2S_8 catholyte yields a large amount of solid S at 2.8 V, which is indeed the cause of its poor cycling reversibility, as will be discussed later. For reference, the as-received pristine carbon paper is shown in Figure S25.

The distinct reduction peaks of $mP_2S_5-nLi_2S_x$ complexes in CV correspond to discrete groups of reactions leading to the successive consumption of Li⁺ by the catholyte materials and, hence, the successive shortening of the sulfur chains. An indepth understanding of reactions that occur at each major reduction activity helps to reveal the underlying discharge mechanism. Specifically, four types of electrochemical reactions were considered for the complex catholyte during discharge (see the Methods section). The corresponding electrochemical potentials were calculated using DFT with $S_{x=8}$ chains as initial reactants and are matched to the experimental CV results, as presented in Table 1. The highest voltage reduction peak at 2.4 V corresponds to long-chain complexes being split into two shorter chains in a process that often produces Li_2S_x . In the second peak at 2.27 V, the reduced S_x chains shortened further, producing short-chain complexes and Li₂S₂. Similarly, at 2.09 V, short-chain complexes and Li₂S are produced. And finally, the remaining short-chain polysulfides are reduced to Li₂S at 1.84 V. Even though Li₂S is predicted to form upon discharge, it would be readily anchored onto the P-S backbone instead of being precipitated out, as demonstrated in Figure 2d and Figures S22 and S23. Electrochemical reactions for the Li₂S₈ system are also presented in Table 1 for comparison. The Li₂S₈ system features a similar mechanism, with long polysulfide chains undergoing successive shortening and eventually producing Li₂S at 1.9 V. In both systems upon discharge, the voltage in the CV scan is ramped down at a given rate, and because reactions occur also at a finite rate, the current density is expected to be observed at a somewhat lower voltage than the electrochemical potential at which reactions were initiated. Therefore, not only the voltage corresponding to peak current density but also the voltage corresponding to the onset of each reduction peak is included in Table 1. Reactions with electrochemical potentials smaller than or equal to that onset voltage are considered for every major peak. The complete set of reactions and their calculated electrochemical potentials can be found in Tables S5-S7.

Cell Performance Evaluation. Figure 3a shows the galvanostatic cycling of battery cells with different catholyte solutions at 0.2 C. The loading of the active material is \sim 1.1 mg cm⁻² unless otherwise mentioned. The complex catholytes exhibit good cycling stability, high specific capacity, and sustained capacity retention as opposed to the Li₂S₈ catholyte, which shows a rapid decay of the capacity to <200 mAh g⁻¹ after 200 cycles. The 3P₂S₅-2Li₂S₈ complex is superior to P₂S₅-Li₂S₈, achieving a high specific capacity of 1425 mAh g⁻¹ and remains at 1270 mAh g⁻¹ over 200 cycles at the C rate tested. This superior performance is attributed to the existence of sufficient phosphorus in the 3:2 stoichiometry to fully accommodate all active sulfur, as discussed earlier, which has been converted to Li₂S in the discharged state. The theoretical capacity that can be delivered by the complex catholyte (based on active sulfur) is 7/8 of 1672 mAh g^{-1} (i.e., 1463 mAh g^{-1}),

Table 1. Discharge Mechanism for $mP_2S_5-nLi_2S_8$ and Li_2S_8 Chemistries⁴

	$P_2S_5-Li_2S_8$	
observed peak (onset), V	2.37 (2.63)	2.27 (2.37)
calculated potential, V	$P^3-S_8-P^3 \rightarrow P^3-S_4-P^3 + Li_2S_4$ (2.51)	$P^{3}-S_{6}-Li \rightarrow P^{3}-S_{4}-Li + Li_{2}S_{2} (2.23)$
	$P^3-S_8-P^3 \rightarrow P^3-S_5-P^3 + Li_2S_3$ (2.38)	$P^3-S_5-P^3 \rightarrow P^3-S_3-P^3 + Li_2S_2 (2.31)$
	$P^3-S_8-P^3 \rightarrow P^3-S_6-Li + P^3-S_2-Li (2.51)$	$P^3-S_4-P^3 \rightarrow P^3-S_2-P^3 + Li_2S_2 (2.28)$
	$P^3-S_8-P^3 \to 2 P^3-S_4-Li$ (2.34)	$P^{3}-S_{2}-Li \rightarrow P^{2}-S-Li + Li$ (2.27)
	P^3 -S ₈ -Li $\rightarrow P^3$ -S ₂ -Li + Li ₂ S ₆ (2.63)	$P^3-S_5-Li \rightarrow P^3-S_3-Li + Li_2S_2 (2.35)$
	$P^3-S_8-Li \rightarrow P^3-S_3-Li + Li_2S_5$ (2.56)	$\text{Li}_2S_6 \rightarrow 2 \text{ Li}_2S_3 (2.28)$
	P^3 -S ₈ -Li $\rightarrow P^3$ -S ₄ -Li + Li ₂ S ₄ (2.47)	
	$P^3-S_8-Li \rightarrow P^3-S_5-Li + Li_2S_3$ (2.36)	
	$P^3-S_6-Li \rightarrow P^3-S_3-Li + Li_2S_3$ (2.45)	
observed peak (onset), V	2.09 (2.15)	1.84 (2.00)
calculated potential, V	$P^3-S_3-P^3 \rightarrow P^3-S_2-P^3 + Li_2S$ (2.01)	$\begin{array}{c} \text{Li}_2S_3 \rightarrow \text{Li}_2S_2 + \text{Li}_2S \\ (1.89) \end{array}$
	$P^3-S_2-P^3 \rightarrow P^3-S-P^3 + Li_2S$ (2.02)	$\text{Li}_2S_2 \to 2 \text{ Li}_2S (1.78)$
	$P^3-S_4-Li \rightarrow P^3-S_3-Li + Li_2S$ (2.10)	
	$P^3-S_3-Li \rightarrow P^3-S_2-Li + Li_2S$ (2.09)	
	$\begin{array}{c} \text{Li}_2\text{S}_5 \rightarrow \text{Li}_2\text{S}_3 + \text{Li}_2\text{S}_2 \\ \text{(2.14)} \end{array}$	
	Li_2S_8	
observed peak (onset), V	2.35 (2.53)	2.14 (2.21)
calculated potential, V	$\text{Li}_2\text{S}_8 \rightarrow 2\text{Li}_2\text{S}_4 (2.45)$	$\begin{array}{c} \operatorname{Li}_2S_5 \to \operatorname{Li}_2S_3 + \operatorname{Li}_2S_2 \\ \text{(2.15)} \end{array}$
	$\begin{array}{c} \text{Li}_2S_8 \rightarrow \text{Li}_2S_5 + \text{Li}_2S_3 \\ \text{(2.35)} \end{array}$	
observed peak (onset), V	1.92 (2.01)	
calculated potential, V	$Li_2S_4 \rightarrow 2Li_2S_2 \ (2.02)$	
	$\text{Li}_2S_3 \rightarrow \text{Li}_2S_2 + \text{Li}_2S$ (1.88)	
	$\text{Li}_2\text{S}_2 \rightarrow 2\text{Li}_2\text{S} \ (1.78)$	

"Individual reactions, with corresponding calculated electrochemical potentials stated in parentheses, are assigned to each electrochemical reduction peak observed in CV experiments. The voltage at peak current density and the voltage at the onset of the peak upon discharge are stated. All reactions are written with 2Li_n and 2Li_{n-1} omitted from the reactants and products, respectively, for brevity.

considering the charged state is equivalent to Li_2S_8 instead of solid sulfur, as supported by the lack of sulfur precipitation on the carbon paper (see Figures S22 and S23). Interestingly, both $3P_2S_5-2\text{Li}_2S_8$ and $P_2S_5-\text{Li}_2S_8$ complexes experienced an activation period in order to realize their full capacity potential, as the capacity rises slightly in the initial 100 cycles in all cases. The cause is probably the gradually enhanced interfacial wetting, as the complex solutions are relatively viscous (Figure S27). Because of excess P_2S_5 , the cycling performance of $2P_2S_5-\text{Li}_2S_8$ is slightly inferior to the $3P_2S_5-\text{2Li}_2S_8$ and $P_2S_5-\text{Li}_2S_8$ complexes (Figure S28). Note that P_2S_5 itself does not directly offer any electrochemical activity (Figure S29).

Electrochemical impedance spectroscopy (EIS) analyses of the complex and Li₂S₈ catholytes are reported in Figure S30. Cells with different catholytes were scanned after the 10th, 50th, and 100th cycles, showing characteristic semicircles in the high-to-middle frequency regions as well as an inclined diffusion tail in the low-frequency region. 50,51 Based on the equivalent circuit model proposed in Figure S30, the highfrequency intercept at the real axis reflects the internal ohmic impedance (R_e) associated with the electrolyte, and the semicircles in the high-to-middle frequency regions correspond to the surface film resistance (R_f) and the charge-transfer resistance (R_{ct}) of cells, respectively.⁵¹ Other components in the equivalent circuit include a constant phase element (CPE) for double-layer capacitance as well as the Warburg impedance $(Z_{\rm w})$ and another CPE for space charge capacitance (CPE').⁵¹ From the fitting results, the 3P₂S₅-2Li₂S₈ complex shows smaller impedance values in comparison to the P_2S_5 -Li $_2S_8$ complex after 10 cycles. More importantly, both $3P_2S_5-2Li_2S_8$ and P₂S₅-Li₂S₈ complexes exhibit lower charge-transfer resistances than the Li₂S₈ catholytes over extended cycles, indicating improved charge-transfer kinetics in complex-based catholytes due to their ability to accommodate Li₂S₂/Li₂S. Moreover, distinct diffusion tails can be observed for the complexes (especially for $3P_2S_5-2Li_2S_8$), which suggests fast Li⁺ transport in the bulk solution, as this is also consistently observed in the Randles-Sevcik analysis of Li+ diffusion properties (Figure S18). In contrast, it is difficult to distinguish the diffusion tail of the Li₂S₈ catholyte due to its sluggish diffusion kinetics.

Post-mortem surface characterization of catholyte substrates provides further evidence about the superior electrochemical reversibility of complexes compared with the Li₂S₈ catholyte (Figure 3b). Carbon paper substrates with the 3P₂S₅-2Li₂S₈ and P₂S₅-Li₂S₈ complexes remain nearly pristine after 50 cycles, with a weak S signal that possibly originates from adsorbed soluble complexes. This confirms that the complexation can effectively prevent the solid discharge products from precipitating during battery operation and significantly extend the battery's cycle life. In contrast, the surface of the carbon paper substrate dissembled from the Li₂S₈ cell displays a large amount of solid precipitates after 50 cycles, thus explaining its fast capacity decay and poor cycle life. The complete elemental mapping information can be found in Figures S31-S33. A schematic illustrating the distinct cycling reversibility between complex and Li₂S₈ catholyte is presented in Figure S34.

To examine any potential negative effects (e.g., byproducts or contamination) resulting from the introduction of P₂S₅ on the anode, we further conducted SEM and X-ray photoelectron spectroscopy (XPS) characterization of Li metal anodes paired with different catholyte solutions after 50 cycles. As shown in Figure S35, both 3P₂S₅-2Li₂S₈ and P₂S₅-Li₂S₈ catholytes lead to more compact and homogeneous Li deposition compared to the Li₂S₈ catholyte without P₂S₅ complexation. In particular, severe whisker-like dendrite growth is observed with the Li₂S₈ catholyte, while such dendrite growth is absent in the 3P₂S₅-2Li₂S₈ and P₂S₅-Li₂S₈ catholytes. These distinct surface morphologies are closely related to the interfacial chemistries and the solid electrolyte interface (SEI) compositions (Figure S36). Specifically, similar C_{1s} spectra are observed, suggesting electrolyte decomposition on the Li metal surface with and without P_2S_5 complexation. With complexation, however, a strong phosphorus peak (132.6 eV) is observed in the P_{2p} spectra and can be attributed to the PS₄³⁻ group, which is

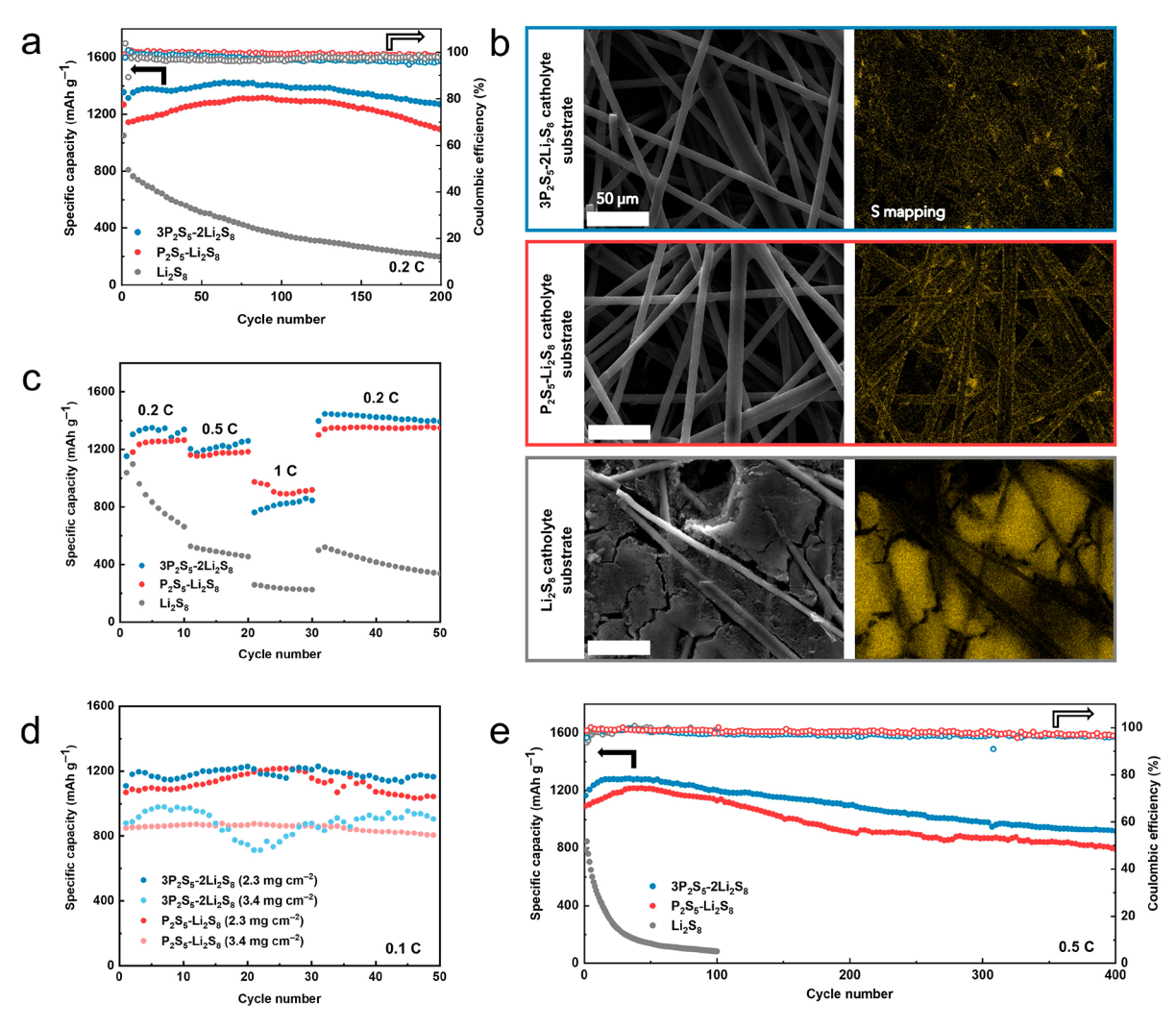


Figure 3. Room temperature battery performance evaluation. (a) Galvanostatic cycling of cells with $3P_2S_5-2Li_2S_8$, $P_2S_5-Li_2S_8$, and Li_2S_8 catholytes at 0.2 C. (b) SEM images and corresponding S mappings of $3P_2S_5-2Li_2S_8$, $P_2S_5-Li_2S_8$, and Li_2S_8 catholyte substrates dissembled after 50 cycles at the discharged state. (c) Rate performance of $3P_2S_5-2Li_2S_8$, $P_2S_5-Li_2S_8$, and Li_2S_8 catholytes over a range of active material loadings. (e) Long-term cycling of cells with $3P_2S_5-2Li_2S_8$, $P_2S_5-Li_2S_8$, and Li_2S_8 catholytes at 0.5 C.

known to be a superionic conductor that facilitates stable Li plating. All Because species with binding energy <132 eV in the P_{2p} spectra are absent, we can exclude potential risks associated with P_2S_5 reduction. The formation of Li_3PS_4 can be supported also by the P=S group (161.6 eV) and the Li-P-S group (163.5 eV) in the S_{2p} spectra. In contrast, the S_{2p} spectra of Li metal without P_2S_5 complexation indicate the formation of short-chain sulfur species as a result of uncontrolled polysulfide reduction. The remaining peaks (with binding energy above 165 eV) in the S_{2p} spectra are from the decomposition of sulfone species in lithium bis(trifluoromethanesulfonyl)imide (LiTFSI), which can be found in both the complexes and Li_2S_8 systems.

With regard to the rate performance (Figure 3c), $3P_2S_5 - 2Li_2S_8$ delivers capacities of 1350, 1258, and 860 mAh g⁻¹ at 0.2, 0.5, and 1 C, respectively, and the capacity rises back to 1435 mAh g⁻¹ when operated again at 0.2 C at room temperature. Similarly, the capacities of $P_2S_5 - Li_2S_8$ are 1264, 1184, 975, and 1350 mAh g⁻¹ at 0.2, 0.5, 1, and 0.2 C, respectively. In contrast, the Li_2S_8 catholyte shows weak rate performance with a significant capacity reduction due to

irreversible polysulfide dissolution and Li₂S precipitation at every cycle. Unlike complex-based catholytes, the Li₂S₈ catholyte experienced fast capacity decay even after the rate is returned to 0.2 C. As shown in Figure 3d, both 3P₂S₅-2Li₂S₈ and P₂S₅-Li₂S₈ complexes exhibit reasonably good cycling performance when the active material loading was increased to 2.3 and 3.4 mg cm⁻² from the baseline of 1.1 mg cm⁻². The long-term cycling of the complex and Li₂S₈ catholytes at 0.5 C is presented in Figure 3e. The 3P₂S₅-2Li₂S₈ complex achieves 80% capacity retention after 400 cycles, while the P_2S_5 -Li₂S₈ complex is at 72%. In contrast, the Li₂S₈ catholyte experienced a drastic capacity decay and failed within 100 cycles. As shown in Figure S37, the long-term cycling of complex catholytes is also evaluated at 1 C. At this C-rate, the 3P₂S₅-2Li₂S₈ complex exhibits somewhat inferior performance to the stoichiometric P_2S_5 -Li₂S₈ catholyte. This behavior is also observed in Figure 3c. The performance of the 3P₂S₅-2Li₂S₈ complex at 1 C is probably hampered by an increased viscosity (Figure S27) and decreased ionic conductivity (Figure S38) compared to the P₂S₅-Li₂S₈

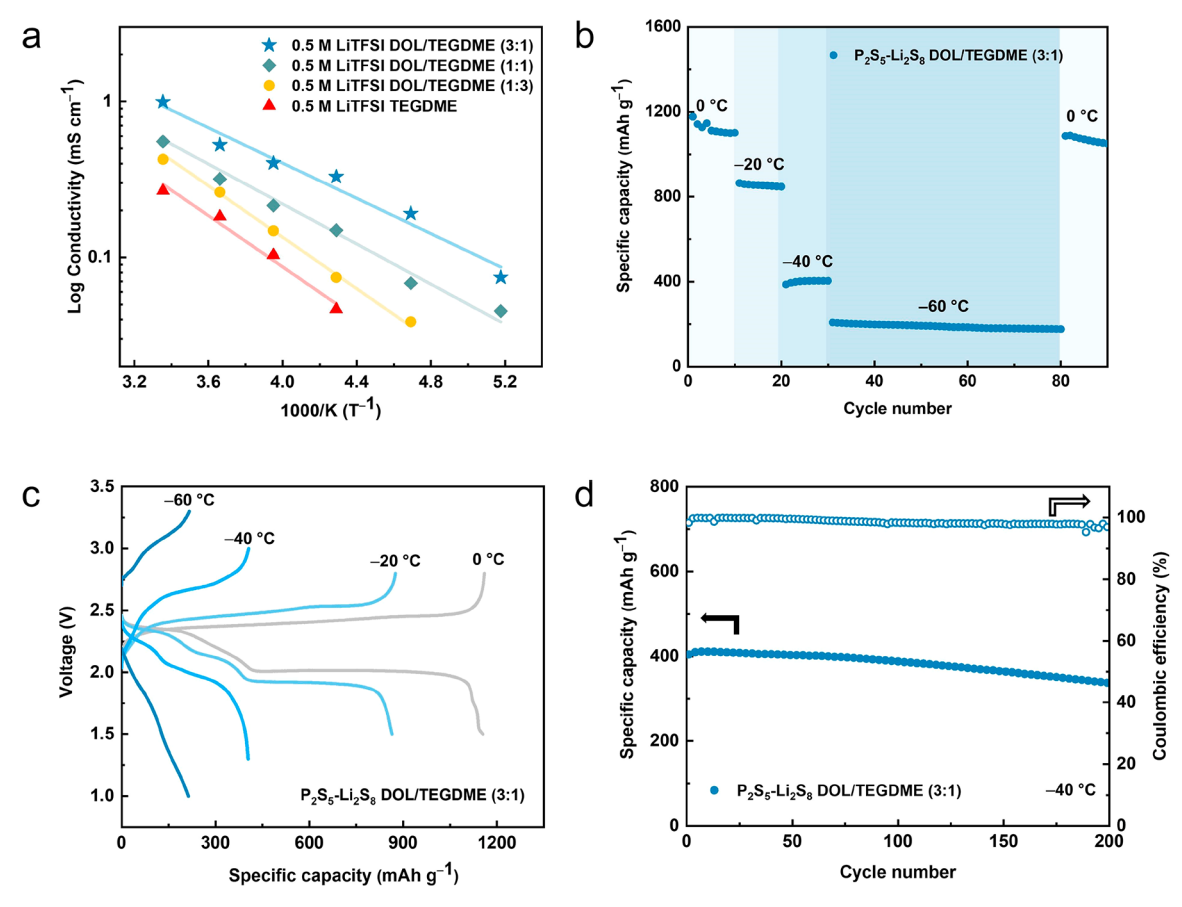


Figure 4. Low-temperature battery performance evaluation. (a) Temperature-dependent ionic conductivity of 0.5 M LiTFSI in different combinations of TEGDME and DOL between 25 and -80 °C. (b) Temperature-dependent galvanostatic cycling of cell with $P_2S_5-Li_2S_8$ in DOL/TEGDME (3:1) at 0.1 C from 0 to -60 °C. (c) Corresponding galvanostatic charge–discharge voltage profiles at 0.1 C from 0 to -60 °C. (d) Long-term cycling of cell with $P_2S_5-Li_2S_8$ in DOL/TEGDME (3:1) at 0.1 C and -40 °C.

complex. This problem may be addressed by optimizing the solvent or the substrate design in the future. ^{33,51,53,54}

Low-Temperature Performance Evaluation. In addition to the significantly improved reversibility of complexes at room temperature, the cell performance was further evaluated at reduced temperatures to evaluate the response of the cell performance to temperature variations. Because TEGDME has a relatively high melting point (-30 °C) and large viscosity (3.4 mPa·s), 55 it is unfavorable for low-temperature applications. 1,3-Dioxolane (DOL), an essential electrolyte component in conventional Li-S batteries, 56,57 is employed instead as a cosolvent for the complexes owing to its low melting point (-95 °C) and low viscosity (0.59 mPa·s),⁵⁸ both of which are beneficial to the low-temperature operation. In particular, the low viscosity of DOL is expected to reduce the viscosity of the DOL-TEGDME mixture and hence maintain a reasonable level of ion conduction at reduced temperatures. Figure 4a shows the temperature-dependent ionic conductivity of 0.5 M LiTFSI in different volume ratios of TEGDME and DOL. The higher DOL content (e.g., 75 vol %) tends to give higher ionic conductivities across the temperature range of 25 to -80 °C. However, due to the reduced solubility of polysulfides (and hence the complexes) in DOL,⁵⁷ further increasing the DOL content beyond 80 vol % would limit battery performance. Moreover, decreasing the operating temperature also impacts the complex solubility. As shown in Figure S39, both $3P_2S_5-2Li_2S_8$ and $P_2S_5-Li_2S_8$ complexes exhibit good solubility in 75 vol % DOL and 25 vol %

TEGDME (i.e., DOL/TEGDME (3:1)) at room temperature, but solid precipitation starts to occur for the $3P_2S_5-2Li_2S_8$ complex below -35 °C. As such, here we demonstrate the low-temperature battery performance with $P_2S_5-Li_2S_8$ in DOL/TEGDME (3:1) only. Note that the addition of DOL does not change the complex structure, as the same characteristic P-SROs are all still present in the ^{31}P NMR spectra (Figure S40). ^{1}H NMR characterization of $P_2S_5-Li_2S_8$ in DOL/TEGDME (3:1) (Figure S41) also does not show any side reactions due to DOL addition.

P₂S₅-Li₂S₈ in DOL/TEGDME (3:1) delivers reasonably high capacities of 1177, 864, 404, and 208 mAh g^{-1} at 0.1 C and 0, -20, -40, and -60 °C, respectively (Figure 4b). This suggests that the low-temperature operability of the P₂S₅-Li₂S₈ catholyte is improved by the addition of DOL. Also, the capacity loss from the temperature step-down is recoverable as the temperature rises back to 0 °C from −60 °C. As shown in Figure 4c, even at a temperature as low as −40 °C, distinct charge/discharge plateaus can still be observed. Because of slower reaction kinetics toward low temperatures, cell electrochemical windows are extended from 1.5-2.8 V (0 and -20 °C) to 1.3-3.0 V (-40 °C) and eventually 1.0-3.3 V (-60 °C) in order to improve the charge/discharge capacity in each case. Long-term cycling retains 83% of the initial capacity (405 mAh g^{-1}) over 200 cycles for P_2S_5 -Li₂S₈ in DOL/ TEGDME (3:1) at 0.1 C and -40 °C, as shown in Figure 4d. These results indicate a further advantage associated with the complexation chemistry, as it offers a key solution to

overcoming the kinetic and reversibility limitations that plague conventional Li–S batteries. Note that such superior wide-temperature electrochemical performance of complexes catholytes has not been reported in previous lithium–sulfur battery studies using liquid sulfur cathodes (catholytes). A detailed comparison of performance between the current study and reported literature can be found in Table S10.

CONCLUSIONS

We developed a series of lithium thiophosphate $(mP_2S_5$ $n \text{Li}_2 S_x$) complexes in TEGDME as promising catholytes for Li-S batteries. Various degrees of optimization, including sulfur chain length, complexation stoichiometry, and solvent selection, are demonstrated to render complexes with distinctive solubility and attractive electrochemical properties. Insights garnered from the coupled spectroscopic and DFT studies enable the formulation of the complex structures, the complexation mechanism, and the associated electrochemical reaction mechanism. We show that the complexation provides a host molecular structure that can effectively accommodate discharge reaction products that would otherwise precipitate out of the solvent without complexation. Therefore, major issues associated with Li₂S₂/Li₂S production in lithium-sulfur batteries, such as sluggish redox kinetics, volume expansion, and voltage-polarization, are mended. The 3P₂S₅-2Li₂S₈ complex was predicted theoretically and confirmed experimentally to exhibit superior battery performance with high specific capacity (1425 mAh g⁻¹ at 0.2 C) and excellent cycling stability (80% retention after 400 cycles at 0.5 C) at room temperature. Low-temperature performance observed with DOL as a cosolvent (>400 mAh g^{-1} at -40 °C and >200 mAh g^{-1} at -60 °C) is equally encouraging. Overall, this work suggests a new route to liquid-sulfur-based cathodes with excellent Li₂S₂/Li₂S solubilities to improve the reversibility, stability, cycling performance, and low-temperature capabilities of Li-S batteries.

ASSOCIATED CONTENT

Supporting Information

The Supporting Information is available free of charge at https://pubs.acs.org/doi/10.1021/jacs.3c05209.

Details of materials, chemicals, and methods used in this work, including the preparation of catholyte solutions, electrochemical measurements, materials characterizations, DFT calculations, as well as supplementary figures and tables (PDF)

AUTHOR INFORMATION

Corresponding Authors

Hai Wang — Department of Mechanical Engineering, Stanford University, Stanford, California 94305, United States; Email: haiwang@stanford.edu

Weiyang Li — Thayer School of Engineering, Dartmouth College, Hanover, New Hampshire 03755, United States; orcid.org/0000-0001-5827-415X; Email: weiyang.li@dartmouth.edu

Authors

Peiyu Wang — Thayer School of Engineering, Dartmouth College, Hanover, New Hampshire 03755, United States; orcid.org/0000-0001-5986-635X

Nikolaos Kateris — Department of Mechanical Engineering, Stanford University, Stanford, California 94305, United States; © orcid.org/0000-0001-5045-4295

Baiheng Li — Thayer School of Engineering, Dartmouth College, Hanover, New Hampshire 03755, United States Yiwen Zhang — Thayer School of Engineering, Dartmouth College, Hanover, New Hampshire 03755, United States Jianmin Luo — Thayer School of Engineering, Dartmouth College, Hanover, New Hampshire 03755, United States; orcid.org/0000-0002-6233-4140

Chuanlong Wang – Thayer School of Engineering, Dartmouth College, Hanover, New Hampshire 03755, United States

Yue Zhang — Department of Mechanical Engineering, Stanford University, Stanford, California 94305, United States;
orcid.org/0000-0002-7342-7457

Amitesh S. Jayaraman – Department of Mechanical Engineering, Stanford University, Stanford, California 94305, United States

Xiaofei Hu — Thayer School of Engineering, Dartmouth College, Hanover, New Hampshire 03755, United States; orcid.org/0000-0002-9924-2776

Complete contact information is available at: https://pubs.acs.org/10.1021/jacs.3c05209

Author Contributions

P.W. and N.K. contributed equally to this work.

Notes

The authors declare no competing financial interest.

ACKNOWLEDGMENTS

The work at Dartmouth College (W.L.) was partially supported by the Air Force Office of Scientific Research under Grant FA9550-22-1-0143 for the fundamental chemistry and theory development. W.L. also acknowledges the partial support under PE 0603734A, "Energy and Technology Research in Cold and Arctic Regions," Task 2 under Contract W913E519C0008 and under PE 0633119, "Energy and Technology Research in Cold and Arctic Regions," Task 2 under Contract W913E520C0010, both managed by the US Army Engineer Research and Development Center (ERDC) as well as partial support by National Science Foundation program "NNA Track 1: Innovations in Energy Technologies and Empowerment in Arctic Fishing Communities" under Award 1927845. W.L. and P.W. acknowledge the support from Dartmouth PhD innovation program. W.L. also acknowledges the partial support under Camille Dreyfus Teacher-Scholar Award (Award TC-22-008) from the Camille and Henry Dreyfus Foundation. The work at Stanford University (H.W.) was partially supported by the Air Force Office of Scientific Research under Grants FA9550-19-1-0261 and FA9550-20-1-0398. We acknowledge the assistance of Paul Defino from the Department of Chemistry at Dartmouth College for NMR characterization. We thank Dr. Min Li, Dr. Yiren Zhong, and Dr. Hailiang Wang from Yale University for XPS characterization. Some of the computing for this project was performed on the Stanford Sherlock cluster. We thank the Stanford Research Computing Center for providing computational resources and support that contributed to these research results.

REFERENCES

- (1) Dunn, B.; Kamath, H.; Tarascon, J.-M. Electrical Energy Storage for the Grid: A Battery of Choices. Science 2011, 334, 928-935.
- (2) Cano, Z. P.; Banham, D.; Ye, S.; Hintennach, A.; Lu, J.; Fowler, M.; Chen, Z. Batteries and Fuel Cells for Emerging Electric Vehicle Markets. Nat. Energy 2018, 3, 279-289.
- (3) Yang, Y.; Zheng, G.; Cui, Y. A Membrane-Free Lithium/ Polysulfide Semi-Liquid Battery for Large-Scale Energy Storage. Energy Environ. Sci. 2013, 6, 1552.
- (4) Bruce, P. G.; Freunberger, S. A.; Hardwick, L. J.; Tarascon, J.-M. Li-O2 and Li-S Batteries with High Energy Storage. Nat. Mater. 2012, 11, 19-29.
- (5) Ji, X.; Lee, K. T.; Nazar, L. F. A Highly Ordered Nanostructured Carbon-Sulphur Cathode for Lithium-Sulphur Batteries. Nat. Mater. 2009, 8, 500-506.
- (6) Yang, Y.; Zheng, G.; Cui, Y. Nanostructured Sulfur Cathodes. Chem. Soc. Rev. 2013, 42, 3018.
- (7) Xin, S.; Gu, L.; Zhao, N.-H.; Yin, Y.-X.; Zhou, L.-J.; Guo, Y.-G.; Wan, L.-J. Smaller Sulfur Molecules Promise Better Lithium-Sulfur Batteries. J. Am. Chem. Soc. 2012, 134, 18510-18513.
- (8) Xu, Y.; Wen, Y.; Zhu, Y.; Gaskell, K.; Cychosz, K. A.; Eichhorn, B.; Xu, K.; Wang, C. Confined Sulfur in Microporous Carbon Renders Superior Cycling Stability in Li/S Batteries. Adv. Funct. Mater. 2015, 25, 4312-4320.
- (9) Zhou, Z.; Li, G.; Zhang, J.; Zhao, Y. Wide Working Temperature Range Rechargeable Lithium-Sulfur Batteries: A Critical Review. Adv. Funct. Mater. 2021, 31, 2107136.
- (10) Gupta, A.; Bhargav, A.; Jones, J.-P.; Bugga, R. V.; Manthiram, A. Influence of Lithium Polysulfide Clustering on the Kinetics of Electrochemical Conversion in Lithium-Sulfur Batteries. Chem. Mater. **2020**, 32, 2070-2077.
- (11) Jiao, Y.; Wang, F.; Ma, Y.; Luo, S.; Li, Y.; Hu, A.; He, M.; Li, F.; Chen, D.; Chen, W.; Lei, T.; Hu, Y. Challenges and Advances on Low-Temperature Rechargeable Lithium-Sulfur Batteries. Nano Res. 2023, 16, 8082-8096.
- (12) Yin, Y.-X.; Xin, S.; Guo, Y.-G.; Wan, L.-J. Lithium-Sulfur Batteries: Electrochemistry, Materials, and Prospects. Angew. Chem., *Int. Ed.* **2013**, *52*, 13186–13200.
- (13) Wang, H.; Yang, Y.; Liang, Y.; Robinson, J. T.; Li, Y.; Jackson, A.; Cui, Y.; Dai, H. Graphene-Wrapped Sulfur Particles as a Rechargeable Lithium-Sulfur Battery Cathode Material with High Capacity and Cycling Stability. Nano Lett. 2011, 11, 2644-2647.
- (14) Jayaprakash, N.; Shen, J.; Moganty, S. S.; Corona, A.; Archer, L. A. Porous Hollow Carbon@Sulfur Composites for High-Power Lithium-Sulfur Batteries. Angew. Chem. 2011, 123, 6026-6030.
- (15) Zheng, G.; Yang, Y.; Cha, J. J.; Hong, S. S.; Cui, Y. Hollow Carbon Nanofiber-Encapsulated Sulfur Cathodes for High Specific Capacity Rechargeable Lithium Batteries. Nano Lett. 2011, 11, 4462-4467.
- (16) Wei, S.; Ma, L.; Hendrickson, K. E.; Tu, Z.; Archer, L. A. Metal-Sulfur Battery Cathodes Based on PAN-Sulfur Composites. J. Am. Chem. Soc. 2015, 137, 12143-12152.
- (17) Pang, Q.; Kundu, D.; Cuisinier, M.; Nazar, L. F. Surface-Enhanced Redox Chemistry of Polysulphides on a Metallic and Polar Host for Lithium-Sulphur Batteries. Nat. Commun. 2014, 5, 4759.
- (18) Mi, Y.; Liu, W.; Yang, K. R.; Jiang, J.; Fan, Q.; Weng, Z.; Zhong, Y.; Wu, Z.; Brudvig, G. W.; Batista, V. S.; Zhou, H.; Wang, H. Ferrocene-Promoted Long-Cycle Lithium-Sulfur Batteries. Angew. Chem., Int. Ed. 2016, 55, 14818-14822.
- (19) Zhang, S. S. Role of LiNO3 in Rechargeable Lithium/Sulfur Battery. Electrochim. Acta 2012, 70, 344-348.
- (20) Li, W.; Yao, H.; Yan, K.; Zheng, G.; Liang, Z.; Chiang, Y.-M.; Cui, Y. The Synergetic Effect of Lithium Polysulfide and Lithium Nitrate to Prevent Lithium Dendrite Growth. Nat. Commun. 2015, 6,
- (21) Zhao, C.-X.; Li, X.-Y.; Zhao, M.; Chen, Z.-X.; Song, Y.-W.; Chen, W.-J.; Liu, J.-N.; Wang, B.; Zhang, X.-Q.; Chen, C.-M.; Li, B.-Q; Huang, J.-Q; Zhang, Q. Semi-Immobilized Molecular Electro-

- catalysts for High-Performance Lithium-Sulfur Batteries. J. Am. Chem. Soc. 2021, 143, 19865-19872.
- (22) Zhong, Y.; Yin, L.; He, P.; Liu, W.; Wu, Z.; Wang, H. Surface Chemistry in Cobalt Phosphide-Stabilized Lithium-Sulfur Batteries. J. Am. Chem. Soc. 2018, 140, 1455-1459.
- (23) Shi, H.; Ren, X.; Lu, J.; Dong, C.; Liu, J.; Yang, Q.; Chen, J.; Wu, Z. Dual-functional Atomic Zinc Decorated Hollow Carbon Nanoreactors for Kinetically Accelerated Polysulfides Conversion and Dendrite Free Lithium Sulfur Batteries. Adv. Energy Mater. 2020, 10, 2002271.
- (24) Shi, H.; Qin, J.; Lu, P.; Dong, C.; He, J.; Chou, X.; Das, P.; Wang, J.; Zhang, L.; Wu, Z. Interfacial Engineering of Bifunctional Niobium (V)-based Heterostructure Nanosheet toward High Efficiency Lean-electrolyte Lithium-Sulfur Full Batteries. Adv. Funct. Mater. 2021, 31, 2102314.
- (25) Burns, D. A.; Baumann, A. E.; Bennett, K. J.; Díaz, J. C.; Thoi, V. S. Chemical Sulfide Tethering Improves Low-Temperature Li-S Battery Cycling. ACS Appl. Mater. Interfaces 2021, 13, 50862-50868.
- (26) Burns, D. A.; Benavidez, A.; Buckner, J. L.; Thoi, V. S. Maleimide-Functionalized Metal-Organic Framework for Polysulfide Tethering in Lithium-Sulfur Batteries. Mater. Adv. 2021, 2, 2966-
- (27) Baumann, A. E.; Han, X.; Butala, M. M.; Thoi, V. S. Lithium Thiophosphate Functionalized Zirconium Mofs for Li-S Batteries with Enhanced Rate Capabilities. J. Am. Chem. Soc. 2019, 141, 17891-
- (28) Haldar, S.; Wang, M.; Bhauriyal, P.; Hazra, A.; Khan, A. H.; Bon, V.; Isaacs, M. A.; De, A.; Shupletsov, L.; Boenke, T.; et al. Porous Dithiine-Linked Covalent Organic Framework as a Dynamic Platform for Covalent Polysulfide Anchoring in Lithium-Sulfur Battery Cathodes. J. Am. Chem. Soc. 2022, 144, 9101-9112.
- (29) Cheon, S.-E.; Choi, S.-S.; Han, J.-S.; Choi, Y.-S.; Jung, B.-H.; Lim, H. S. Capacity Fading Mechanisms on Cycling a High-Capacity Secondary Sulfur Cathode. J. Electrochem. Soc. 2004, 151, A2067.
- (30) Seh, Z. W.; Li, W.; Cha, J. J.; Zheng, G.; Yang, Y.; McDowell, M. T.; Hsu, P.-C.; Cui, Y. Sulphur-TiO₂ Yolk-Shell Nanoarchitecture with Internal Void Space for Long-Cycle Lithium-Sulphur Batteries. Nat. Commun. 2013, 4, 1331.
- (31) Yuan, Y.; Tan, G.; Wen, J.; Lu, J.; Ma, L.; Liu, C.; Zuo, X.; Shahbazian-Yassar, R.; Wu, T.; Amine, K. Encapsulating Various Sulfur Allotropes within Graphene Nanocages for Long-Lasting Lithium Storage. Adv. Funct. Mater. 2018, 28, 1706443.
- (32) Pan, H.; Han, K. S.; Vijayakumar, M.; Xiao, J.; Cao, R.; Chen, J.; Zhang, J.; Mueller, K. T.; Shao, Y.; Liu, J. Ammonium Additives to Dissolve Lithium Sulfide through Hydrogen Binding for High-Energy Lithium-Sulfur Batteries. ACS Appl. Mater. Interfaces 2017, 9, 4290-4295.
- (33) Cheng, Q.; Xu, W.; Qin, S.; Das, S.; Jin, T.; Li, A.; Li, A. C.; Qie, B.; Yao, P.; Zhai, H.; Shi, C.; Yong, X.; Yang, Y. Full Dissolution of the Whole Lithium Sulfide Family (Li2S8 to Li2S) in a Safe Eutectic Solvent for Rechargeable Lithium-Sulfur Batteries. Angew. Chem., Int. Ed. 2019, 58, 5557-5561.
- (34) Stephens, P. J.; Devlin, F. J.; Chabalowski, C. F.; Frisch, M. J. Ab Initio Calculation of Vibrational Absorption and Circular Dichroism Spectra using Density Functional Force Fields. J. Phys. Chem. 1994, 98, 11623-11627.
- (35) Francl, M. M.; Pietro, W. J.; Hehre, W. J.; Binkley, J. S.; Gordon, M. S.; DeFrees, D. J.; Pople, J. A. Self-consistent Molecular Orbital Methods. XXIII. A Polarization-type Basis Set for Second-row Elements. J. Chem. Phys. 1982, 77, 3654-3665.
- (36) Gordon, M. S.; Binkley, J. S.; Pople, J. A.; Pietro, W. J.; Hehre, W. J. Self-consistent Molecular-orbital Methods. 22. Small Splitvalence Basis Sets for Second-row Elements. J. Am. Chem. Soc. 1982, 104, 2797-2803.
- (37) Spitznagel, G. W.; Clark, T.; von Rague Schleyer, P.; Hehre, W. J. An Evaluation of the Performance of Diffuse Function-augmented Basis Sets for Second Row Elements, Na-Cl. J. Comput. Chem. 1987, 8, 1109-1116.

- (38) Frisch, M. J.; Pople, J. A.; Binkley, J. S. Self-consistent Molecular Orbital Methods 25. Supplementary Functions for Gaussian Basis Sets. *J. Chem. Phys.* **1984**, *80*, 3265–3269.
- (39) Eckert, H.; Zhang, Z.; Kennedy, J. H. Structural Transformation of Non-Oxide Chalcogenide Glasses. the Short-Range Order of Lithium Sulfide (Li2S)-Phosphorus Pentasulfide (P2SS) Glasses Studied by Quantitative Phosphorus-31, Lithium-6, and Lithium-7 High-Resolution Solid-State NMR. *Chem. Mater.* **1990**, 2, 273–279.
- (40) Dietrich, C.; Weber, D. A.; Sedlmaier, S. J.; Indris, S.; Culver, S. P.; Walter, D.; Janek, J.; Zeier, W. G. Lithium Ion Conductivity in Li2S-P2S5 Glasses Building Units and Local Structure Evolution during the Crystallization of Superionic Conductors Li3PS4, Li7P3S11 and Li4P2S7. *J. Mater. Chem. A* **2017**, *5*, 18111–18119.
- (41) Pang, Q.; Liang, X.; Shyamsunder, A.; Nazar, L. F. An in Vivo Formed Solid Electrolyte Surface Layer Enables Stable Plating of Li Metal. *Joule* **2017**, *1*, 871–886.
- (42) Wang, C.; Zhang, Y.; Zhang, Y.; Luo, J.; Hu, X.; Matios, E.; Crane, J.; Xu, R.; Wang, H.; Li, W. Stable Sodium-Sulfur Electrochemistry Enabled by Phosphorus-Based Complexation. *Proc. Natl. Acad. Sci. U. S. A.* **2021**, *118*, 49.
- (43) Liu, Y.; Elias, Y.; Meng, J.; Aurbach, D.; Zou, R.; Xia, D.; Pang, Q. Electrolyte Solutions Design for Lithium-Sulfur Batteries. *Joule* **2021**, *5*, 2323–2364.
- (44) Hagen, M.; Schiffels, P.; Hammer, M.; Dörfler, S.; Tübke, J.; Hoffmann, M. J.; Althues, H.; Kaskel, S. In-Situ Raman Investigation of Polysulfide Formation in Li-S Cells. *J. Electrochem. Soc.* **2013**, *160*, A1205.
- (45) Bischoff, C.; Schuller, K.; Haynes, M.; Martin, S. W. Structural Investigations of yNa2S + (1-y)PS5/2 Glasses Using Raman and Infrared Spectroscopies. *J. Non-Cryst. Solids.* **2012**, 358, 3216–3222.
- (46) Bischoff, C.; Schuller, K.; Dunlap, N.; Martin, S. W. Ir, Raman, and NMR Studies of the Short-Range Structures of 0.5Na2S + 0.5[xGeS2 + (1-x)PS5/2] Mixed Glass-Former Glasses. *J. Phys. Chem. B* **2014**, *118*, 1943–1953.
- (47) Berbano, S. S.; Seo, I.; Bischoff, C. M.; Schuller, K. E.; Martin, S. W. Formation and Structure of Na2S + P2S5 Amorphous Materials Prepared by Melt-Quenching and Mechanical Milling. *J. Non-Cryst. Solids.* **2012**, 358, 93–98.
- (48) Riadigos, C. F.; Iglesias, R.; Rivas, M. A.; Iglesias, T. P. Permittivity and Density of the Systems (Monoglyme, Diglyme, Triglyme, or Tetraglyme+n-Heptane) at Several Temperatures. *J. Chem. Thermodyn.* **2011**, *43*, 275–283.
- (49) Ghidiu, M.; Ruhl, J.; Culver, S. P.; Zeier, W. G. Solution-Based Synthesis of Lithium Thiophosphate Superionic Conductors for Solid-State Batteries: A Chemistry Perspective. *J. Mater. Chem. A* **2019**, *7*, 17735–17753.
- (50) Qiu, X.; Hua, Q.; Zheng, L.; Dai, Z. Study of the Discharge/Charge Process of Lithium-Sulfur Batteries by Electrochemical Impedance Spectroscopy. *RSC Adv.* **2020**, *10*, 5283–5293.
- (51) Zhou, G.; Paek, E.; Hwang, G. S.; Manthiram, A. Long-Life Li/Polysulphide Batteries with High Sulphur Loading Enabled by Lightweight Three-Dimensional Nitrogen/Sulphur-Codoped Graphene Sponge. *Nat. Commun.* **2015**, *6*, 7760.
- (52) Chu, H.; Noh, H.; Kim, Y.-J.; Yuk, S.; Lee, J.-H.; Lee, J.; Kwack, H.; Kim, Y.; Yang, D.-K.; Kim, H.-T. Achieving Three-Dimensional Lithium Sulfide Growth in Lithium-Sulfur Batteries Using High-Donor-Number Anions. *Nat. Commun.* **2019**, *10*, 188.
- (53) Huang, W.; Wang, P.; Liao, X.; Chen, Y.; Borovilas, J.; Jin, T.; Li, A.; Cheng, Q.; Zhang, Y.; Zhai, H.; Chitu, A.; Shan, Z.; Yang, Y. Mechanically-Robust Structural Lithium-Sulfur Battery with High Energy Density. *Energy Stor.* **2020**, *33*, 416–422.
- (54) Shi, H.; Zhao, X.; Wu, Z.-S.; Dong, Y.; Lu, P.; Chen, J.; Ren, W.; Cheng, H.-M.; Bao, X. Free-Standing Integrated Cathode Derived from 3D Graphene/Carbon Nanotube Aerogels Serving as Binder-Free Sulfur Host and Interlayer for Ultrahigh Volumetric-Energy-Density Lithium Sulfur Batteries. *Nano Energy* **2019**, *60*, 743–751.
- (55) Qian, K.; Seifert, S.; Winans, R. E.; Li, T. Understanding Solvation Behavior of the Saturated Electrolytes with Small/Wide-

- Angle X-Ray Scattering and Raman Spectroscopy. *Energy Fuels* **2021**, 35, 19849–19855.
- (56) Gupta, A.; Bhargav, A.; Manthiram, A. Highly Solvating Electrolytes for Lithium-Sulfur Batteries. *Adv. Energy Mater.* **2019**, *9*, 1803096
- (57) Liu, G.; Sun, Q.; Li, Q.; Zhang, J.; Ming, J. Electrolyte Issues in Lithium-Sulfur Batteries: Development, Prospect, and Challenges. *Energy Fuels* **2021**, *35*, 10405–10427.
- (58) Kaiser, M. R.; Chou, S.; Liu, H. K.; Dou, S. X.; Wang, C.; Wang, J. Structure-Property Relationships of Organic Electrolytes and Their Effects on Li/S Battery Performance. *Adv. Mater.* **2017**, 29, 1700449.